Optical Engineering

OpticalEngineering.SPIEDigitalLibrary.org

Effect of multiorder harmonics in a double-Raman pumped gain medium for a superluminal laser

Ye Wang
Zifan Zhou
Joshua Yablon
Selim Shahriar

SPIE.

Optical Engineering 54(5), 057106 (May 2015)

Effect of multiorder harmonics in a double-Raman pumped gain medium for a superluminal laser

Ye Wang,[a,*] Zifan Zhou,[a] Joshua Yablon,[a] and Selim Shahriar[a,b]
[a]Northwestern University, Department of Electrical Engineering and Computer Science, 2145 Sheridan Road, Evanston, Illinois 60208, United States
[b]Northwestern University, Department of Physics and Astronomy, 2145 Sheridan Road, Evanston, Illinois 60208, United States

Abstract. Use of a double-Raman pump applied to a three-level system is a convenient method for generating negative dispersion. When the gain at the center is high enough, such a system can be used to realize a superluminal laser, which in turn can be used to enhance the sensitivity of rotation sensors. For this condition, it is often necessary to apply strong pumps that are closely spaced in frequency. Accurate modeling of this system thus requires taking into account interference between the two pumps. We present such an analysis where we allow for an arbitrary number of harmonics that result from this interference, and investigate the behavior of the gain profile under a wide range of conditions. We also describe an experimental study of double-Raman gain in a Rb vapor cell, and find close agreement between the experimental result and the theoretical model. The technique reported here can be used in developing a quantitative model of a superluminal laser under wide-ranging conditions. [DOI: 10.1117/1.OE.54.5.057106]

Keywords: double-Raman gain; Λ system; superluminal.

Paper 150308 received Mar. 17, 2015; accepted for publication Apr. 28, 2015; published online May 27, 2015.

1 Introduction

Recently, we have been investigating the development of a superluminal ring laser (SRL).[1–9] Briefly, an SRL is a laser where the group velocity of light far exceeds the vacuum speed of light without violating causality or relativity.[10,11] It is the active version of the white light cavity.[12–16] The spectral sensitivity of laser, defined as the change in frequency as a function of a change in the cavity length, is enhanced by a factor ξ, that can be as high as 10^5 for experimentally realizable parameters.[1] It is also important to take into account another factor, η, defined as the ratio of the quantum noise limited linewidth of an SRL to that of a conventional laser with similar operating parameters, such as mirror reflectivity, cavity length, and output power. The effective enhancement in sensitivity, defined as the minimum measurable change in the cavity length (for application to a range of devices, including gyroscopes, accelerometers, magnetometers, and gravitational wave detectors[1,2,5,9]), is expected to be (ξ/η). It has been suggested previously, with some qualitative arguments,[1,2] that the value of η may be of the order of unity. Some investigations[17,18] have been undertaken to understand the behavior of passive cavities containing dispersive media, in order to shed light on what the value of η might actually be. However, to date, a definitive determination of the value of η remains elusive, both theoretically and experimentally. Physical realization of an SRL is necessary to establish the value of η, thereby determining the extent to which an SRL may enhance sensitivity in metrology.

In an SRL, the enhancement in spectral sensitivity results from the presence of a properly tuned negative dispersion. Broadly speaking, the negative dispersion is achieved by introducing an effective dip in the spectral profile of the gain and operating the laser at the center of this dip. There are many potential ways to realize an SRL, including the use of coupled cavities,[6,7,8,19] dual frequency pumped Brillouin gain,[20] or use of an auxiliary cell inside a diode pumped alkali laser system to produce Raman induced absorption. Yet another approach is to make use of a dual-pumped Raman gain system in atomic vapor,[4,10] which has many potential advantages over the other proposed approaches.

Briefly, the dual pumped Raman gain makes use of a Λ-type transition, easily realizable in an alkali vapor, such as Rubidium. In such a system, an optical pumping beam is employed to create a population imbalance between the two low-lying, metastable states of the Λ system. When an optically detuned pump is applied on the leg that couples the lower level with the higher population to the intermediate level, a probe on the other leg experiences a narrow-band Raman gain with a width of γ, centered at the two-photon resonant frequency of the probe. When another pump is added on the same leg as that of the first pump but is detuned by some frequency Δ, the probe experiences two different gain peaks, separated by Δ. If the value of Δ is chosen to be less than γ, the effective gain profile has a dip in the overall gain profile, which is what is needed for an SRL. A cavity tuned to be resonant at the center of the two Raman gain peaks will thus become an SRL with the proper choice of parameters.

A potential complication in this approach is that when $\Delta < \gamma$, there is interference between the two Raman gain processes, especially when the pumps are made to be strong in order to produce a large gain at the center. Under such a condition, the total gain profile cannot be expressed as a simple sum of the two individual gain profiles.

*Address all correspondence to: Ye Wang, E-mail: yewang@u.northwestern.edu

0091-3286 /2015/$25.00

In this paper, we present a detailed theoretical calculation to predict the exact shape of the gain profile under arbitrary conditions. Since two different frequencies are present on a given transition, the rotating wave transformation[21,22] cannot be used to realize a time independent Hamiltonian. As such, it is necessary to use a perturbative technique whereby the density matrix is expanded to include n harmonies of Δ, where n is chosen to be large enough to produce a converging result. We show numerical result for up to $n = 7$, and find that the gain profile has additional peaks beyond the two expected from the simple model. We also find that, in general, the strengths of the two pumps have to be unequal in order to produce a condition where the two strongest gain peaks become equal. We also present experimental results, obtained with a cell of ^{85}Rb atoms, and show close agreement with the theoretical model.

The rest of the paper is organized as follows. In Sec. 2, we first introduce the double-Raman gain model for the three-level Λ system. We then develop the equations of motion for the elements of the density matrix expanded to an arbitrary number of harmonics of the beat frequency between the two pump beams. We present the steady state solutions of these equations for a wide range of conditions. In Sec. 3, we add velocity averaging into our model, and consider situations where the probe is copropagating or counter-propagating with respect to the pumps. In Sec. 4, we present the details of our experimental realization of a double-Raman gain system, and compare the simulation result with experimental data. We conclude in Sec. 5 with a summary of the paper.

2 Double-Raman Gain System

The basic system we consider for producing the double-Raman gain peaks is illustrated schematically in Fig. 1. Here, level $|1\rangle$ and $|2\rangle$ are assumed to be long-lived ground states, each coupled via electric dipolar transitions to the intermediate states $|3\rangle$ and $|4\rangle$, which are assumed to be far apart in energy. Since the energy difference between $|1\rangle$ and $|2\rangle$ is much less than the thermal energy, ($k_B T$, where k_B is the Boltzmann constant and T is the temperature) at room temperature, the population in these two levels are roughly equal under thermal equilibrium. An optical pumping beam, locked to the $|1\rangle \rightarrow |4\rangle$ transition, is tuned to create a population imbalance between these two states. The effect of this pump is modeled as a net decay rate of Γ_{12} from state $|1\rangle$ to state $|2\rangle$. (Decaying from $|4\rangle \rightarrow |2\rangle$ is implicitly included here.) The Raman pumps with frequencies ω_{p1} and ω_{p2}, respectively, are applied to the $|2\rangle \rightarrow |3\rangle$ transition, each being highly detuned in order to avoid the effect of spontaneous emission. The Rabi frequencies of these two pumps are Ω_{p1} and Ω_{p2}, respectively. The probe beam, at frequency ω_s, is applied to the $|1\rangle \rightarrow |3\rangle$ transition, also highly detuned. We indicate by $\hbar\omega_j$ the energy of the state $|j\rangle$, for $j = (1, 2, 3)$. Δ_p is defined as the detuning of the central frequency of the two Raman pump fields, i.e., $\Delta_p = (\omega_{p1} + \omega_{p2})/2 - (\omega_3 - \omega_2)$. The frequency difference between the two Raman pumps is $\Delta \equiv \omega_{p2} - \omega_{p1}$. The detuning of the probe beam is $\delta = \omega_s - (\omega_3 - \omega_1)$. When $\delta = \Delta_p \pm \Delta/2$, a two-photon transition condition is met. In that case, the Raman probe will experience a gain. In the experiment to be described later, we implemented the Λ system with a ^{85}Rb D1 line, with $|1\rangle$, $|2\rangle$, and $|3\rangle$ corresponding to the $5S_{1/2}$ $F = 2$, $5S_{1/2}$ $F = 3$, and $5P_{1/2}$, respectively, and the D2 transition is used for optical pumping (i.e., $|4\rangle$ is the $5P_{3/2}$ manifold).

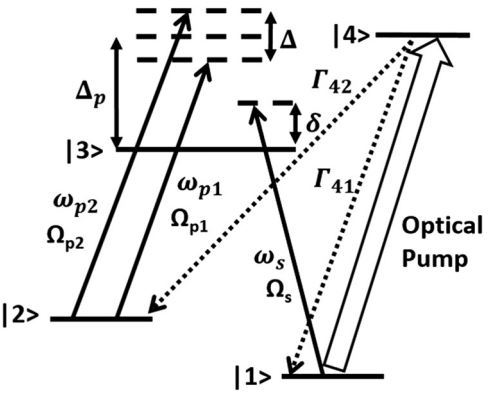

Fig. 1 The double-Raman gain system. Ω_s is the Rabi frequency of the Raman probe. Ω_{p1} and Ω_{p2} are Rabi frequencies of Raman pumps 1 and 2, respectively. Γ_{41} and Γ_{42} are the decay rates from $|4\rangle$ to $|1\rangle$ and $|2\rangle$, respectively.

Under the electric dipole and rotating wave approximation, the Hamiltonian for the system shown in Fig. 1 can be expressed on the basis of $|1\rangle$, $|2\rangle$, and $|3\rangle$, as:

$$\mathcal{H} = \hbar \begin{bmatrix} \omega_1 & 0 & \frac{1}{2} e^{i\omega_s t}\Omega_s \\ 0 & \omega_2 & \left(\frac{1}{2} e^{i\omega_{p1} t}\Omega_{p1} + \frac{1}{2} e^{i\omega_{p2} t}\Omega_{p2}\right) \\ \frac{1}{2} e^{-i\omega_s t}\Omega_s & \left(\frac{1}{2} e^{-i\omega_{p1} t}\Omega_{p1} + \frac{1}{2} e^{-i\omega_{p2} t}\Omega_{p2}\right) & \omega_3 \end{bmatrix}. \quad (1)$$

Here, without loss of generality, we have assumed that the phase of each of the three fields is zero. The gain experienced by the probe is not affected by the relative phases of these fields, since there is no closed loop involved in the interaction.[23]

As can be seen, the term in the Hamiltonian that represents the coupling between $|2\rangle$ and $|3\rangle$ contains two different oscillatory terms. As such, there is no transformation that can convert this into a fully time-independent form. Thus, we choose arbitrarily to carry out a transformation that eliminates the time dependence for only one of the terms. Specifically, the state vector $|\psi\rangle$; is transformed to $|\tilde{\psi}\rangle \equiv Q|\psi\rangle$, where $Q \equiv e^{i\theta_1 t}|1\rangle\langle 1| + e^{i\theta_2 t}|2\rangle\langle 2| + e^{i\theta_3 t}|3\rangle\langle 3|$, and choose $\theta_1 = -\omega_1$, $\theta_2 = -\delta - (\Delta/2) + \Delta_p - \omega_2$, and $\theta_3 = -\delta - \omega_3$. The effective Hamiltonian for $|\tilde{\psi}\rangle$ is then given by Ref. 23:

$$\tilde{\mathcal{H}} = \hbar \begin{bmatrix} 0 & 0 & \frac{\Omega_s}{2} \\ 0 & -\frac{1}{2}(2\delta + \Delta - 2\Delta_p) & \frac{1}{2}(\Omega_{p1} + e^{i\Delta t}\Omega_{p2}) \\ \frac{\Omega_s}{2} & \frac{1}{2}(\Omega_{p1} + e^{-i\Delta t}\Omega_{p2}) & -\delta \end{bmatrix}. \quad (2)$$

The Liouville's equation for the density matrix in this basis can be written as:

$$\frac{d\tilde{\rho}}{dt} = -\frac{i}{\hbar}(\tilde{\tilde{\mathcal{H}}}\tilde{\rho} - \tilde{\rho}\tilde{\tilde{\mathcal{H}}}^{\dagger}) + M_{\text{source}}, \tag{3}$$

where $\tilde{\tilde{\mathcal{H}}}$ is a non-Hermitian Hamiltonian introduced for convenience,[23] and is given by:

$$\tilde{\tilde{\mathcal{H}}} = \tilde{\mathcal{H}} - i\frac{\hbar}{2}(\Gamma_1|\tilde{1}\rangle\langle\tilde{1}| + \Gamma_2|\tilde{2}\rangle\langle\tilde{2}| + \Gamma_3|\tilde{3}\rangle\langle\tilde{3}|), \tag{4}$$

and M_{source} accounts for the influx of population into the three states, which is expressed as:

$$M_{\text{source}} = (\Gamma_{21}\tilde{\rho}_{22} + \Gamma_{31}\tilde{\rho}_{33})|\tilde{1}\rangle\langle\tilde{1}| + (\Gamma_{12}\tilde{\rho}_{11} + \Gamma_{32}\tilde{\rho}_{33})|\tilde{2}\rangle\langle\tilde{2}| + (\Gamma_{13}\tilde{\rho}11 + \Gamma_{23}\tilde{\rho}_{22})|\tilde{3}\rangle\langle\tilde{3}|. \tag{5}$$

Here, Γ_i $(i = 1, 2, 3)$ is the net decay rate of state $|\tilde{i}\rangle$, Γ_{ij} $(i, j = 1, 2, 3)$ is the decay rate from level $|\tilde{i}\rangle$; to level $|\tilde{j}\rangle$, and $\tilde{\rho}_{ij} \equiv \langle\tilde{i}|\tilde{\rho}|\tilde{j}\rangle$. In formulating Eq. (5), we have assumed a closed system, i.e., $\tilde{\rho}_{11} + \tilde{\rho}_{22} + \tilde{\rho}_{33} = 1$.

In general, all the decay rates in Eqs. (4) and (5) could be nonvanishing. However, for one particular system of inherence, we make the following assumptions about these rates. Γ_3 $(= 2\pi \times 6 \times 10^6\ \text{sec}^{-1})$ is the radiation decay rate from level $|3\rangle$, and we assume $\Gamma_{31} = \Gamma_{32} = \Gamma_3/2$. We also assume that $\Gamma_{13} = \Gamma_{23} = 0$. In the absence of optical pumping, $\Gamma_1 = \Gamma_{12}$ and $\Gamma_2 = \Gamma_{21}$ would account for the collisional exchange of populations between $|\tilde{1}\rangle$ and $|\tilde{2}\rangle$, with $\Gamma_1 \cong \Gamma_2$ (of the order of a few kHz) since the population of states $|\tilde{1}\rangle$ and $|\tilde{2}\rangle$ are roughly equal in thermal equilibrium at the operating temperature. However, the effect of the optical pumping via state $|4\rangle$ produced a net decay rate from $|\tilde{1}\rangle$ to $|\tilde{2}\rangle$; that is much stronger than these collisional ratios. Thus, we assume that $\Gamma_2 = \Gamma_{21} = 0$ and $\Gamma_1 = \Gamma_{12} \equiv \Gamma_{\text{op}}$, where Γ_{op} is the rate of optical pumping.

Since some of the coupling terms in the Liouville equation have a periodicity of $(2\pi/\Delta)$, the general solution of the density matrix is an infinite sum which includes stationary components plus all the harmonies (positive + negative) of Δ

$$\tilde{\rho} = \tilde{\rho}^0 + \sum_{n=1}^{\infty}(\tilde{\rho}^{-n}e^{-in\Delta t} + \tilde{\rho}^n e^{in\Delta t}). \tag{6}$$

A characteristic parameter for the strength of the contribution of the n'th order is K_n, defined as the sum of the absolute values of all the elements

$$K_n \equiv \sum_{i=1}^{3}\sum_{j=1}^{3}\{|\tilde{\rho}_{ij}^n| + |\tilde{\rho}_{ij}^{-n}|\}. \tag{7}$$

In general, K_n for a given n would increase monotonically with increasing pump Rabi frequencies. Furthermore, for a fixed set of parameters, K_n would decrease monotonically with increasing n. These patterns can be used as a guide in deciding the maximum value of n to keep in the summation of Eq. (6). Specifically, we will use the convention that

$$\tilde{\rho} = \tilde{\rho}^0 + \sum_{n=1}^{M}(\tilde{\rho}^{-n}e^{-in\Delta t} + \tilde{\rho}^n e^{in\Delta t}), \quad K_M < \varepsilon, \tag{8}$$

where ε can be chosen to have a value that is sufficient for the required accuracy. We will use a value of $\varepsilon = 0.01$ in the results presented here.

It should be noted that Eq. (8) represents a relation for each element of the density matrix

$$\tilde{\rho}_{ij} = \tilde{\rho}_{ij}^0 + \sum_{n=1}^{M}(\tilde{\rho}_{ij}^{-n}e^{-in\Delta t} + \tilde{\rho}_{ij}^n e^{in\Delta t}),$$
$$i = \{1, 2, 3\}, \quad j = \{1, 2, 3\}, \quad K_M < \varepsilon. \tag{9}$$

The Liouville equation [Eq. (3)], when applied to the density matrix of Eq. (8) [or equivalently Eq. (9)], represents a set of coupled differential equations involving 9 variables $\tilde{\rho}_{ij}$ subject to the closed system constraints that $\tilde{\rho}_{11} + \tilde{\rho}_{22} + \tilde{\rho}_{33} = 1$. If we represent the 9 variables as a vector $\vec{A}$ (with the elements ordered in any chosen way), then the Liousville equation can be expressed as $\frac{d\vec{A}}{dt} = M\vec{A}$, where the matrix M is time dependent. As such, this system does not have a steady state solution, even when the closed system constraint is used.

In principle, one can determine the time evolution of $\vec{A}$ via simple numerical integration. However, we are interested in the limit where the system reaches a quasi steady state where the time evolution involves only the harmonics of Δ. In this limit, for all i, j, and $n \le M$, the elements $\tilde{\rho}_{ij}^0$ and $\tilde{\rho}_{ij}^{\pm n}$ become constants. We can then equate terms with the same temporal coefficients in order to derive the values of these elements.

To illustrate this process explicitly, consider, for example, the case of $M = 1$, and focus arbitrarily on $\tilde{\rho}_{12}$. The Liousville equation implies that:

$$\frac{d\tilde{\rho}_{12}}{dt} = -\frac{1}{2}\Gamma_1\tilde{\rho}_{12} - \frac{1}{2}\Gamma_2\tilde{\rho}_{12} - i\delta\tilde{\rho}_{12} - \frac{i}{2}\Delta\tilde{\rho}_{12} + i\Delta_p\tilde{\rho}_{12} + \frac{i}{2}\tilde{\rho}_{13}\Omega_{p1} + \frac{i}{2}e^{-it\Delta}\tilde{\rho}_{13}\Omega_{p2} - \frac{i}{2}\tilde{\rho}_{32}\Omega_s, \tag{10}$$

where $\tilde{\rho}_{12} = \tilde{\rho}_{12}^0 + \tilde{\rho}_{12}^1 e^{i\Delta t} + \tilde{\rho}_{12}^{-1}e^{-i\Delta t}$. In a quasi steady state, $\tilde{\rho}_{12}^0$, $\tilde{\rho}_{12}^1$, and $\tilde{\rho}_{12}^{-1}$ are constants. As such, the left hand side (LHS.) of Eq. (10) becomes

$$\frac{d\tilde{\rho}_{12}}{dt} = 0 + i\Delta\tilde{\rho}_{12}^1 e^{i\Delta t} - i\Delta\tilde{\rho}_{12}^{-1}e^{-i\Delta t}. \tag{11}$$

On the right hand side (RHS), we use the relation that $\tilde{\rho}_{ij} = \tilde{\rho}_{ij}^0 + \tilde{\rho}_{ij}^1 e^{i\Delta t} + \tilde{\rho}_{ij}^{-1}e^{-i\Delta t}$. Furthermore, we use the closed-system constraint that $\tilde{\rho}_{11} + \tilde{\rho}_{22} + \tilde{\rho}_{33} = 1$ in order to eliminate $\tilde{\rho}_{33}$ everywhere. Now, equating the constant terms between the LHS and RHS, we get:

$$0 = -\frac{1}{2}(\tilde{\rho}_{12}^0\Gamma_1) - i\tilde{\rho}_{12}^0\delta + i\Delta_p\tilde{\rho}_{12}^0 + \frac{i}{2}\Omega_{p1}\tilde{\rho}_{13}^0 + \frac{i}{2}\Omega_{p2}\tilde{\rho}_{13}^1 - \frac{1}{2}\tilde{\rho}_{12}^0\Gamma_2 - \frac{i}{2}\Delta\tilde{\rho}_{12}^0 - \frac{i}{2}\tilde{\rho}_{32}^0\Omega_s. \tag{12}$$

Similarly, equating the coefficients of the $e^{i\Delta t}$ terms we get:

$$i\Delta\tilde{\rho}_{12}^{1} = -\frac{1}{2}(\tilde{\rho}_{12}^{1}\Gamma_1) - i\delta\tilde{\rho}_{12}^{1} + i\Delta_p\tilde{\rho}_{12}^{1} + \frac{i}{2}\Omega_{p1}\tilde{\rho}_{13}^{1} - \frac{1}{2}\Gamma_2\tilde{\rho}_{12}^{1} - \frac{i}{2}\Delta\tilde{\rho}_{12}^{1} - \frac{i}{2}\Omega_s\tilde{\rho}_{32}^{1}, \quad (13)$$

and by equating the coefficients of the $e^{-i\Delta t}$ terms we get:

$$-i\Delta\tilde{\rho}_{12}^{-1} = -\frac{1}{2}(\tilde{\rho}_{12}^{-1}\Gamma_1) - i\delta\tilde{\rho}_{12}^{-1} + i\Delta_p\tilde{\rho}_{12}^{-1} + \frac{i}{2}\tilde{\rho}_{13}^{-1}\Omega_{p1} + \frac{i}{2}\Omega_{p2}\tilde{\rho}_{13}^{0} - \frac{1}{2}\Gamma_2\tilde{\rho}_{12}^{-1} - \frac{i}{2}\Delta\tilde{\rho}_{12}^{-1} - \frac{i}{2}\tilde{\rho}_{32}^{-1}\Omega_s. \quad (14)$$

The same process can be used to generate these questions corresponding to each element, $\tilde{\rho}_{ij}$ of the density matrix. However, because of the closed system constraint, the equations resulting from $\tilde{\rho}_{33}$ are redundant. As such, we get 24 different equations, which can be easily solved via simple matrix inversion. For a general value of M, we set $8 \times (2M + 1)$ different equations, which can be solved in the same manner.

The solution of the density matrix is then used to determine the gain and dispersion experienced by the probe beam. To do so, we note first that the probe field can be expressed as:

$$\vec{E}_{\text{signal}} = \hat{\epsilon}E_0\cos(kz - \omega_s t), \quad (15)$$

where the polarization, $\hat{\epsilon}$, is chosen to be orthogonal to that of the pump, due to the selection rules for the Raman transition we have employed experimentally. The polarization density at the frequency of the probe can be expressed as (at $z = 0$, for simplicity, without loss of generality):

$$\vec{P}_{s(z=0)} = \epsilon_0\chi\vec{E}_{(z=0)} = \frac{1}{2}\hat{\epsilon}\epsilon_0\chi E_0(e^{i\omega_s t} + e^{-i\omega_s t}). \quad (16)$$

The total polarization density is given by

$$\vec{P}_{\text{total}} = -N|e|\langle\vec{r}\rangle, \quad (17)$$

where N is the density of the atoms, $|e|$ is the electron charge (assuming that a single electron is responsible for the interaction, which is valid for alkali atoms), and $\vec{r}$ is the position of the electron with respect to the nucleus of the atom.

The polarization density responsible for the electric susceptibility of the probe, given in Eq. (16), is the component at frequency ω_s of the following quantity:

$$\vec{P}_\epsilon = -N|e|\langle r_\epsilon\rangle\hat{\epsilon}; \quad r_\epsilon = \vec{r}\cdot\hat{\epsilon}. \quad (18)$$

We assume that $\langle 1|r_\epsilon|3\rangle = \langle 3|r_\epsilon|1\rangle \equiv r_{13}$, $\langle 2|r_\epsilon|3\rangle = \langle 3|r_\epsilon|2\rangle \equiv r_{23}$, and $\langle 1|r_\epsilon|2\rangle = \langle 2|r_\epsilon|1\rangle \equiv 0$. The value of $\langle r_\epsilon\rangle$ is then given by

$$\langle r_\epsilon\rangle = \text{tr}(\rho r_\epsilon) = r_{13}(\rho_{13} + \rho_{31}) + r_{23}(\rho_{23} + \rho_{32}). \quad (19)$$

For our system, ρ_{23} and ρ_{32} correspond to oscillation that are at frequencies far away from ω_s. As such, only ρ_{13} and ρ_{31} will contribute to the polarization density in Eq. (16). In the presence of dual Raman pumps, ρ_{13} and ρ_{31} will have components at ω_s, as well as at $\omega_s \pm n\Delta$. However, only the components of ρ_{13} and ρ_{31} at ω_s will contribute to the polarization density of Eq. (16). Explicitly, we note that

$$\rho_{13} = \tilde{\rho}_{13}e^{-i\omega_s t} = \tilde{\rho}_{13}^{0}e^{-i\omega_s t} + \sum_{n=1}^{M}[\tilde{\rho}_{13}^{-n}e^{-i(\omega_s - n\Delta)t} + \tilde{\rho}_{13}^{n}e^{-i(\omega_s + n\Delta)t}], \quad (20)$$

$$\rho_{31} = \tilde{\rho}_{31}e^{i\omega_s t} = \tilde{\rho}_{31}^{0}e^{i\omega_s t} + \sum_{n=1}^{M}[\tilde{\rho}_{31}^{-n}e^{-i(\omega_s - n\Delta)t} + \tilde{\rho}_{31}^{n}e^{-i(\omega_s + n\Delta)t}]. \quad (21)$$

Thus, the parameter χ in Eq. (16) can be expressed as:

$$\chi = -\frac{2r_{13}\tilde{\rho}_{13}^{0}}{\epsilon_0 E_0}N|e|. \quad (22)$$

Noting that $\Omega_s \equiv |e|r_{13}E_0/\hbar$, we get

$$\chi = \frac{2N\hbar\Omega_s}{\epsilon_0 E_0^2}\tilde{\rho}_{13}^{0}. \quad (23)$$

The gain experienced by the probe can be expressed as $G = e^{-\alpha L}$, where $\alpha = (1/2)k_0\,\text{Im}(\chi)$ and L is the length of the media. The phase delay experienced by the probe is $\Phi = (1/2)k_0\,\text{Re}(\chi)L$.

Before showing the response of the complete system, we first illustrate the individual effect of each Raman pump on the gain seen by the probe. In Fig. 2(a), we show the probe gain in the absence of the higher frequency Raman pump. For convenience, we have chosen $N = 2.5 \times 10^{16}$ m^{-3}, $L = 0.1$ m, $\Omega_s = 0.5\Gamma_3$, $\Gamma_{12} = 0.5\Gamma_3$, and $k_0 = 8.06 * 10^6$ m^{-1}, corresponding to the D2 manifold in Rb. For $\Omega_{p1} = 5\Gamma_3$, we see a peak gain of ~1.7. As the pump strength is increased to $20\Gamma_3$, gain is increased to ~9.8. It should be noted that the peak is slightly shifted to the right from the two-photon resonant condition due to the light shift experienced by level 1. This shift becomes more prominent for higher pump powers. The amount of light shift agrees with the expected value of $\Omega_{p1}^2/4\delta_1$, where $\delta_1 \equiv (\Delta_p - \Delta/2)$ is the detuning of this pump. Figure 2(b) shows the corresponding plots in the absence of the lower frequency Raman pump. The peak gains observed for both cases are the same for the same pump power, as expected.

Next, we consider the case where both pumps are present simultaneously. A typical set of probe gain plots are shown in Fig. 3 as a function of probe detuning. We set $\Delta = \Gamma_3$, $\Delta_p = 200\Gamma_3$, $\Omega_s = 0.5\Gamma_3$, $N = 2.5 \times 10^{16}$ m^{-3}, $L = 0.1$ m, $M = 7$. The figure shows the cases when $\Omega_{p1} = \Omega_{p2} = \Gamma_3$, $2\Gamma_3$, $3\Gamma_3$ and $4\Gamma_3$, respectively. The gain profile shows equal peaks when $\Omega_{p1} = \Omega_{p2} = \Gamma_3$. As the Rabi frequency becomes stronger, the second gain peak becomes larger. The imbalance becomes more significant when Ω_p are further increased.

In Fig. 4, we set $\Omega_{p1} = 5\Gamma_3$ and change the value of Ω_{p2}, while all the other parameters are kept the same as those in Fig. 3. Figures 4(a)–4(d) show the cases when $\Omega_{p2} = \Gamma_3$, $3\Gamma_3$, $4\Gamma_3$, $5\Gamma_3$, respectively. It should be noted that the

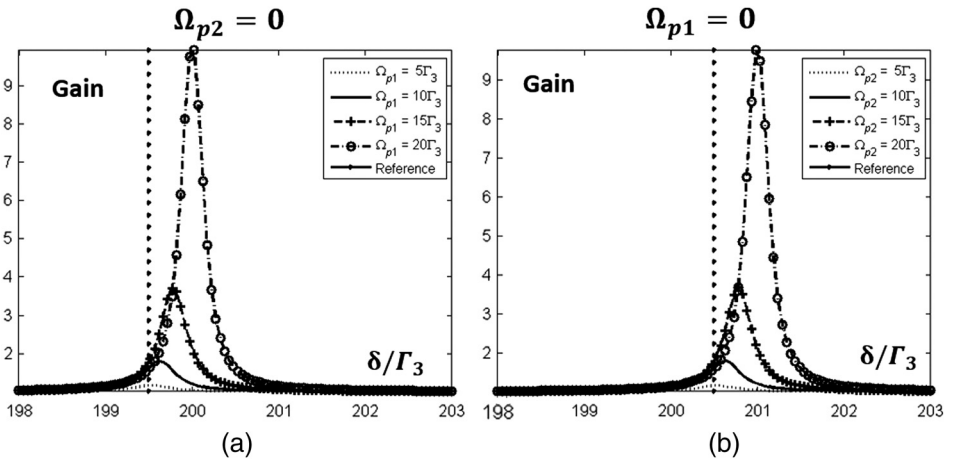

Fig. 2 Illustration of individual Raman gain profiles and effects of light shift: (a) the higher frequency Raman pump is turned off and (b) the lower frequency Raman pump is turned off. The location of the gain peaks moves with increasing pump power due to light shift (or the ac-Stark shift). The reference line in both plots indicates the positions where the gain peak should be without considering light shift. See text for additional details.

peak corresponding to the second pump becomes larger [Fig. 4(d)] than that corresponding to the first pump when $\Omega_{p2} = \Omega_{p1}$. Figure 5 shows the case where all the other parameters are the same as those in Fig. 4, but $\Omega_{p2} = 5\Gamma_3$ and Ω_{p1} is increased from Γ_3 to $5\Gamma_3$. As can be seen, the ratio of the peaks of the two gains follows a pattern that is similar to those in Fig. 4.

We have also verified that this imbalance is reproduced when pumps are detuned below resonance. Specifically, the pump that is further detuned from state $|3\rangle$ is more efficient in producing gain. Obviously, the exact nature of this imbalance depends on the choice of parameters, such as the difference detuning Δ, the mean detuning Δ_p, and the absolute strengths of the pumps. This rather surprising result is due to the complicated interplay between the various higher order terms. It shows that the simple model generally used[6] for double-Raman gain, where the gain spectrum is expressed simply as the sum of two independent Lorentzians, is invalid. Rather, the more comprehensive model presented here must be used in determining the actual gain spectrum.

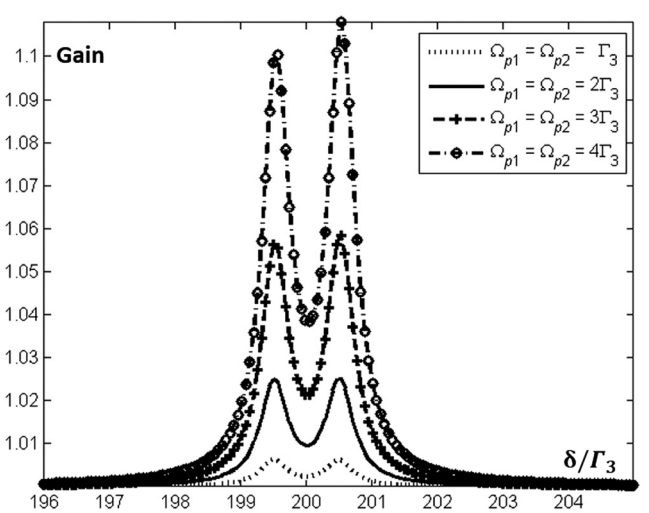

Fig. 3 Illustration of the changes in the Raman gain profile while the pump Rabi frequencies, kept equal to each other, are increased.

Next, we compare the results obtained by the double-Raman code with those produced by the single Raman pump model, which does not require expansion into many orders since the Hamiltonian after the Q transformation becomes time independent. The first comparison we made is to compare the single Raman result with the double-Raman result by setting one Raman pump Rabi frequency to be zero. This is illustrated in Fig. 6, where we plot both the probe gain and the phase delay as a function of the probe frequency. Figure 6(a) shows the result of the single Raman model. We set $\Omega_p = 20\Gamma_3$, $\Delta_p = 199\Gamma_3$, $\Gamma_{12} = 0.5\Gamma_3$, $\Omega_s = 0.5\Gamma_3$, $L = 0.1$ m, and $N = 2.5 \times 10^{16}$ m^{-3}. Figure 6(b) shows the result of the single Raman model by setting $\Delta_p = 201\Gamma_3$ while keeping all the other parameters the same. Figure 6(c) shows the result of the

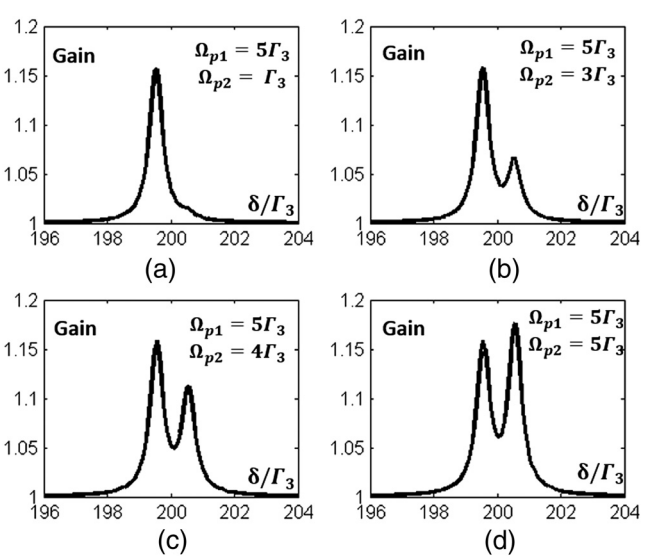

Fig. 4 Illustration of the changes in the gain profile when the second Raman pump Rabi frequency is increased, while keeping the first Raman pump Rabi frequency fixed. Plots (a), (b), (c) and (d) correspond to the cases of $\Omega_{p2}/\Gamma_3 = 1, 3, 4$ and 5 respectively, with $\Omega_{p1}/\Gamma_3 = 5$ in each case.

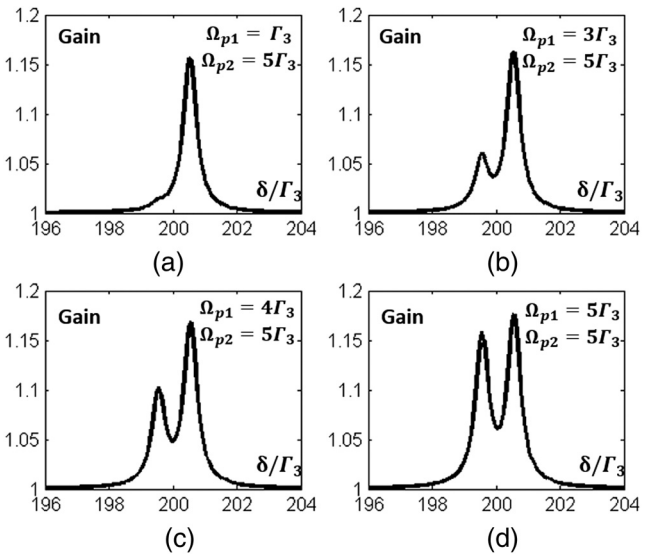

Fig. 5 Illustration of the change in the gain profile when the first Raman pump Rabi frequency is varied, while keeping the second Raman pump Rabi frequency fixed. Plots (a), (b), (c) and (d) correspond to the cases of $\Omega_{p1}/\Gamma_3 = 1, 3, 4$ and 5 respectively, with $\Omega_{p2}/\Gamma_3 = 5$ in each case.

double-Raman model by setting $\Omega_{p1} = 20\Gamma_3$, $\Omega_{p2} = 0$, $\Delta_p = 200\Gamma_3$, $\Delta = 2\Gamma_3$ (recall that the two photon transition happens when $\delta = \Delta_p \pm \Delta/2$), and keeping all the other parameters the same as Fig. 6(a). Figure 6(d) shows the result of the double-Raman model by setting $\Omega_{p1} = 0$, $\Omega_{p2} = 20\Gamma_3$, and keeping all the other parameters the same as Fig. 6(b). The figures demonstrate that the single Raman code and double-Raman code return the same result when one of the Raman pump Rabi frequencies is set to be zero in the double-Raman code.

We also considered the limiting case where $\Delta \to 0$, and compared the result with those obtained using the single Raman model. As $\Delta \to 0$, Eq. (23) is no longer valid. All the harmonics and zero order terms are at the same frequency. In this case, we set $\chi = (2N\hbar\Omega_s/\epsilon_0 E_0^2)[\tilde{\rho}_{13}^0 + \sum_{n=1}^{M}(\tilde{\rho}_{13}^{-n}e^{-in\Delta t} + \tilde{\rho}_{13}^{n}e^{in\Delta t})]$. This is illustrated in Fig. 7. In the double-Raman model, we set $\Omega_{p1} = \Omega_{p2} = 20\Gamma_3$, $\Omega_s = 0.01\Gamma_3$, $\Delta_p = 110\Gamma_3$, $\Delta = 0$, $\Gamma_{12} = \Gamma_3$, $L = 0.1$ m, $N = 2.5 \times 10^{16}$ m^{-3}. Figures 7(a)–7(g) shows the results of the double-Raman simulation by setting $M = 1$, 2, 3, 6, 13, 20, and 30, respectively. Figure 7(h) shows the single Raman case, where we keep all the other parameters the same but set $\Omega_p = 40\Gamma_3$. Ripples are observed on the left side of the phase delay when M is small. As the order M increases, the ripples diminish and the double-Raman model shows closer results compared with the single Raman model.

3 Effect of Velocity Averaging

Next, we consider the effect of velocity distribution, which is important for realizing the double-Raman gain in a vapor cell. We consider first the case where the two pumps as well as the probe are propagating in the same direction. We assume a Maxwell–Boltzmann distribution for the velocities of the atoms. The temperature of the cell is assumed to be 373 K. The specific atom we consider is ^{87}Rb. The length of the cell is assumed to be 0.1 m, at a density of 5×10^{17} m^{-3}.

Figure 8 shows the modification of the gain profile due to the velocity averaging for $\Delta = \Gamma_3$, $\Omega_{p1} = \Omega_{p2} = 2\Gamma_3$, $\Omega_s = 0.01\Gamma_3$, $\Delta_p = 200\Gamma_3$, $\Gamma_{12} = 0.5\Gamma_3$, $N = 5\times10^{17}$ m^{-3}, and $L = 0.1$, where we have used only the first order

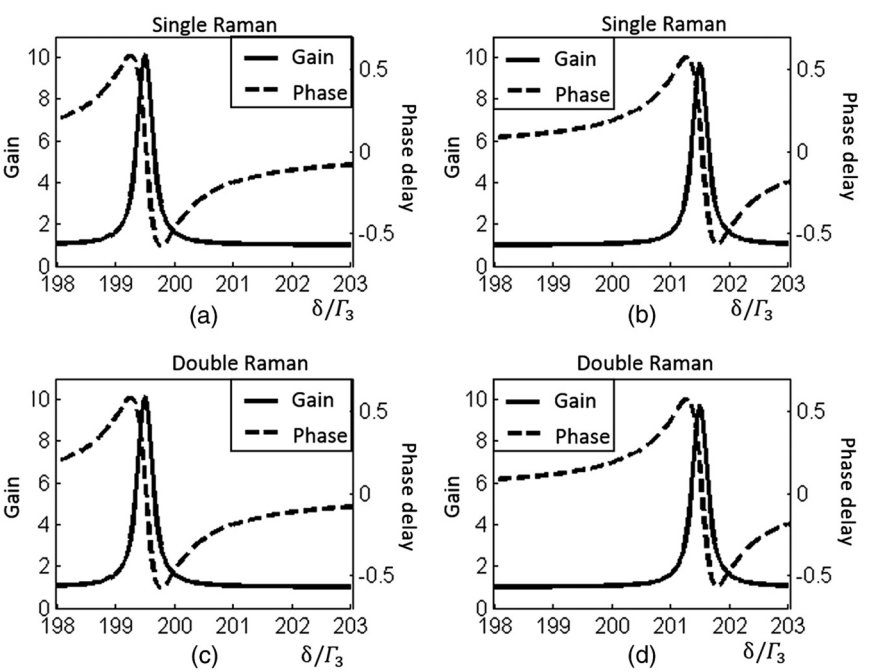

Fig. 6 Comparison between double-Raman gain model and single Raman gain model by setting one Raman pump Rabi frequency to be zero. The plots show the gain (left axis) and the phase delay (right axis) as a function of probe detuning δ: (a) the single Raman model with $\Delta_p = 199\Gamma_3$; (b) the single Raman model with $\Delta_p = 201\Gamma_3$; (c) the double-Raman model with the second Raman pump turned off; and (d) the double-Raman model with the first Raman pump turned off.

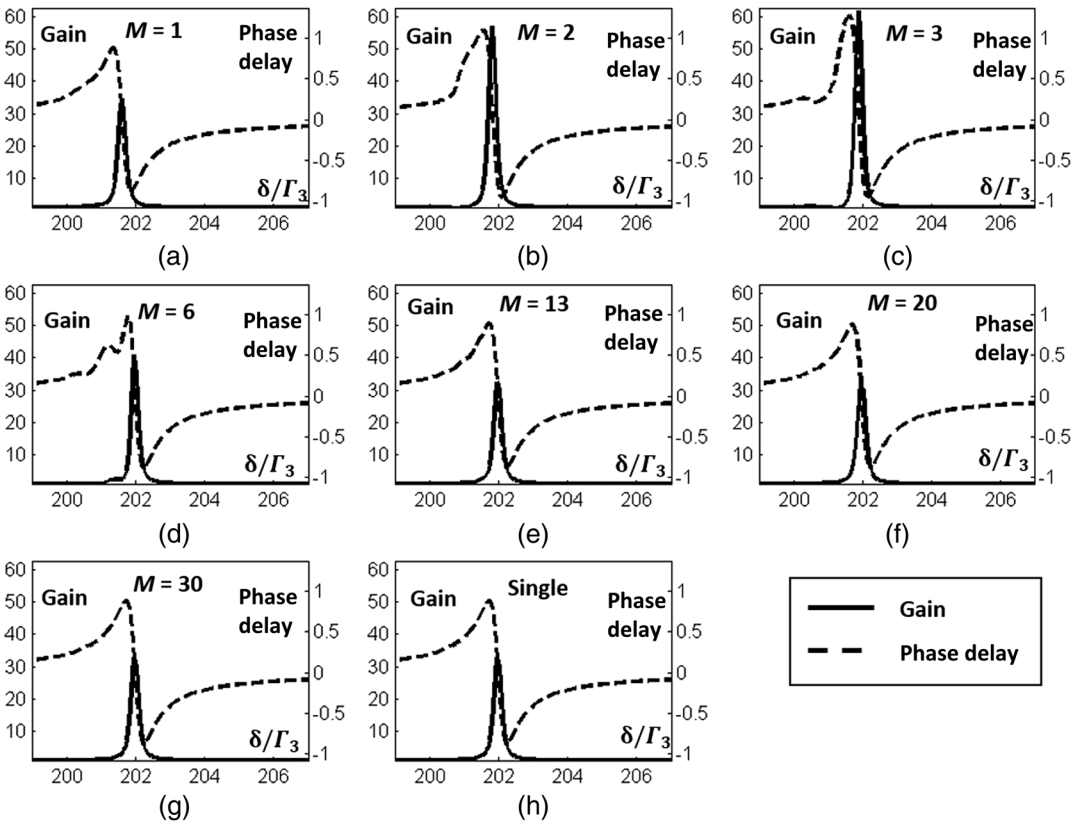

Fig. 7 Comparison between double-Raman gain model and single Raman gain model by setting Δ to be zero. Plots (a)–(g) are generated by the double-Raman model with order numbers of 1, 2, 3, 6, 13, 20, and 30, respectively, while plot (h) is generated by the single Raman model with the same parameters.

expansion ($M = 1$). Figure 8(a) shows the gain as a function of δ/Γ_3. Figure 8(b) shows the phase delay as a function of δ/Γ_3. As can be seen, the averaging produces only a small reduction in the gain, in keeping with the well-known Doppler-shift insensitivity of copropagating Raman interaction.

Next, we consider the case where the two pumps are copropagating, but the probe is propagating in the opposite direction. Physically, it is expected that the efficient gain in this case would come only for the zeros' velocity band. Therefore, the next gain averaged over the velocity profile should be much smaller than that for the copropagating case. This is indeed found to be the case, as shown in Fig. 9.

We consider next the saturation of the gain as a function of the probe power. Such a saturation is important in determining the steady-state property of a laser based on this gain profile. First, we consider the case where only a single Raman pump is present. This is illustrated in Fig. 10. Here, we have used $\Omega_p = 2\Gamma_3$, $\Delta_p = 200\Gamma_3$, $N = 5 \times 10^{17}$ m^{-3}, $L = 0.1$ m, $\Gamma_{12} = 0.5\Gamma_3$. Figures 10(a)–10(c) show gain decreasing as the probe Rabi frequency is increased from $\Omega_s = 0.01\Gamma_3$ to $\Omega_s = 100\Gamma_3$. Figure 10(d) shows the peak gain as a function of $\log(\Omega_s/\Gamma_3)$. The vertical line indicates the saturation point which occurs when the Raman coupling rate matches the optical pumping rate $\Omega_s\Omega_p/(2\Delta_p) = \Gamma_{12}$, which corresponds to $\Omega_s = 2\Gamma_3$.

Next, we show the gain saturation process for the case of double-Raman pumps. Here, the gain value of most interest for realizing a superluminal laser is the one at the center. The results are shown in Fig. 11, where we have used $\Omega_{p1} = \Omega_{p2} = 2\Gamma_3$, $\Delta = \Gamma_3$, $\Delta_p = 200\Gamma_3$, $N = 5 \times 10^{17}$ m^{-3}, $L = 0.1$ m, $M = 6$, and $\Gamma_{12} = 0.5\Gamma_3$. Figures 11(a)–11(c) show three cases where Ω_s is changed from $0.01\Gamma_3$ to $100\Gamma_3$. Figure 11(d) shows the center gain as a function of Ω_s. Again, as expected, the gain saturates when $\Omega_s(\Omega_{p1} + \Omega_{p2})/(2\Delta_p) = \Gamma_{12}$, as indicated by the vertical line.

4 Comparison with Experimental Data

We used a room-temperature cell of ^{85}Rb atoms to carry out the experimental investigation of the double-Raman gain. The transition used is illustrated schematically in Fig. 12. As shown in Fig. 12(a), the two Raman pumps, at frequencies f_{P1} and f_{P2}, are tuned slightly above the $5S_{1/2}$, $F = 3 \rightarrow 5P_{1/2}$ transition. The frequency difference between these is denoted as $\Delta = f_{p2} - f_{p1}$. The probe beam, at frequency f_S, is applied along the $5S_{1/2}$, $F = 2 \rightarrow 5P_{1/2}$ transition. The optical pumping is tuned to the $5S_{1/2}$, $F = 2 \rightarrow 5P_{3/2}$ transition. Figure 12(b) shows the selective position of the frequency f_{P1} with respect to a set of reference transitions in the D1 (~795 nm) manifold, observed using a cell containing a natural mixture of ^{87}Rb and ^{85}Rb. Here, the A and D lines correspond to a transition in ^{87}Rb, the B line corresponds to the $5S_{1/2}$, $F = 3 \rightarrow 5P_{1/2}$ transition and the C line corresponds to the $5S_{1/2}$, $F = 2 \rightarrow 5P_{1/2}$ transition in ^{85}Rb. As can be seen, the frequency f_{P1} is tuned just above the Doppler profile of the B line.

Figure 13 schematically shows the experimental setup. A Ti:Sapphire laser is used to generate the Raman pumps and the Raman probe. A part of the laser output is split off with a nonpolarizing beam splitter (NPBS1), and passed through

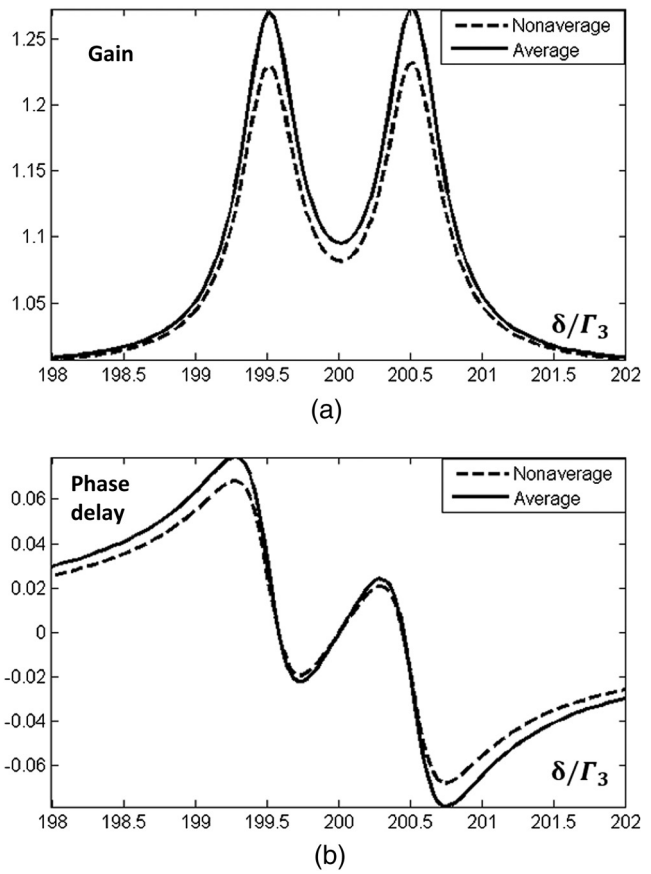

Fig. 8 Comparison between velocity averaging model and nonaveraging model. Plots (a) and (b) show the gain and phase delay, respectively, as a function of δ/Γ_3, where the solid (dashed) line represent the averaging (nonaveraging) model.

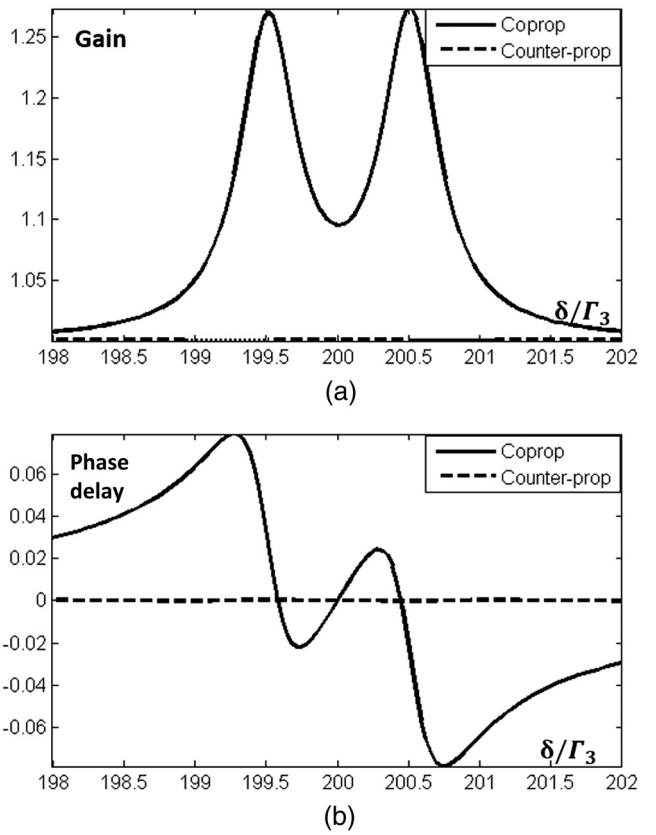

Fig. 9 Comparison between copropagating and counter-propagating cases. Plots (a) and (b) show the gain and phase delay, respectively, as a function of δ/Γ_3, where the solid (dashed) line represent the copropagating (counter-propagating) case.

a reference vapor cell (Rb Cell 1). The laser frequency was scanned by applying a driving voltage $V_D = V_B + V_{\mathrm{SAW}}$, where V_B is a bias voltage, and V_{SAW} is a sawtooth ramp ranging from $-|Vm|$ to $|Vm|$. The value of V_B was adjusted until the frequency of the laser at the zero-crossing point of V_{SAW} was found to be just above the $5S_{1/2}, F = 3 \rightarrow 5P_{1/2}$ transition in ^{85}Rb [as shown in Fig. 12(b)]. The sawtooth ramp was then disconnected, thus parking the laser frequency at this point, denoted as f_{P2}. The Raman gain profile measurement was periodically interrupted, and the sawtooth was reconnected to ensure that the laser frequency remained at the same position. The Ti:Sapphire laser was stable enough so that only a minor adjustment of V_B was needed over the whole experimental period. The laser beam transmitted through NPBS1 was then passed through a half-wave plate (HWP), followed by a polarizing beam splitter (PBS1). The angle of the HWP was adjusted as needed to control the amount of light reflected by PBS1. The light transmitted through PBS1 was passed through NPBS2. The light transmitted through NPBS2 was passed through an acousto-optic modulator (AOM3), driven by a voltage controlled oscillator at frequency f_{AOM3}. The value of f_{AOM3} was set nominally at half the frequency difference (~3.034 GHz) between the $F = 2$ and $F = 3$ states in the $5S_{1/2}$ manifold of ^{85}Rb. The light upshifted in frequency by f_{AOM3} was than reflected back and passed through the AOM3 again, thus producing light at frequency f_S, the Raman probe frequency. The value of f_S could be scanned across the two-photon resonant condition for each Raman pump by tuning the value of f_{AOM3}. The field at f_S, emerging from AOM3 upon reflection, was then reflected partially by

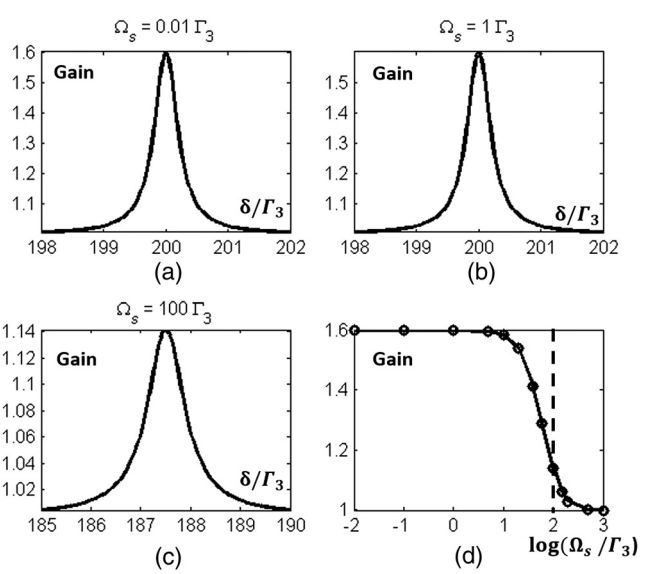

Fig. 10 Illustration of gain saturation in the case of a single Raman gain: (a)–(c) the gain profile for three different probe Rabi frequencies and (d) the peak value of gain as a function of increasing probe Rabi frequency. The dashed vertical line indicates the position where the Raman transition rate equals the optical pumping rate.

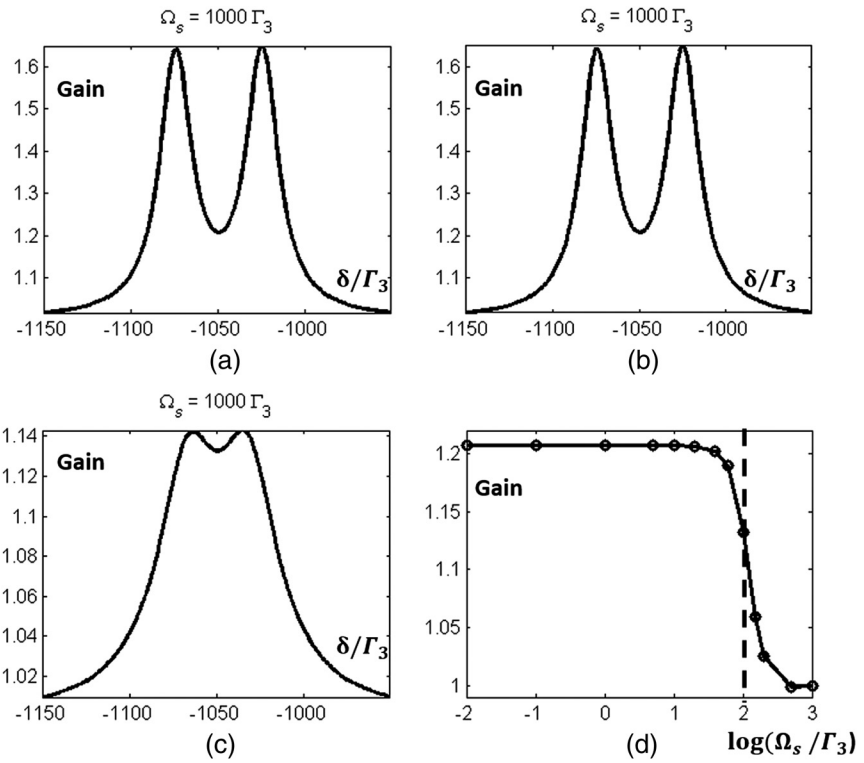

Fig. 11 Illustration of gain saturation in the case of double-Raman gain: (a)–(c) the gain profile for three different probe Rabi frequencies and (d) the gain at the center of the profile as a function of the probe Rabi frequency. The dashed vertical line corresponds to the points where the Raman transition rate equals the optical pumping rate.

NPBS2 and directed into the primary cell (Rb Cell 2) used for producing the Raman gain.

The light reflected by PBS1 was passed through three consecutive beam splitters (NPBS3, NPBS4 and NPBS2) and also sent to the primary cell. This served as one of the Raman pumps at frequency f_{P2}. Light reflected by NPBS3 was passed through two sequential AOMs (AOM1 and AOM2), configured so that AOM1 shifted the frequency up by f_{AOM1}, and AOM2 shifted the frequency down by f_{AOM3}, thus producing the second Raman pump at frequency f_{P1}. Thus, we have $\Delta = f_{P1} - f_{P2} = f_{\mathrm{AOM1}} - f_{\mathrm{AOM2}}$. The value of Δ was tuned as necessary by changing both f_{AOM1} and f_{AOM2}. The beam at frequency f_{P1}, emerging from AOM2, was then reflected by NPBS4 and then passed through NPBS2, entering the primary cell (Rb Cell 2), while copropagating with the other Raman pump as well as the probe. Note that the two Raman pumps have the same (linear) polarization, while the probe polarization is orthogonal to that of the pumps. Upon exiting the primary cell, the beams were passed through another PBS (PBS2), thus separating the probe from the pumps. The transmitted probe power was monitored with a photodetector.

The beam necessary for the optical pumping, at frequency f_{OP}, was generated from a different laser system: a diode laser combined with a tapered amplifier. A part of the light from this laser was reflected by a beam-splitter (NPBS5) and passed through another reference Rb cell (Rb cell 3). The same technique as described above was used to ensure

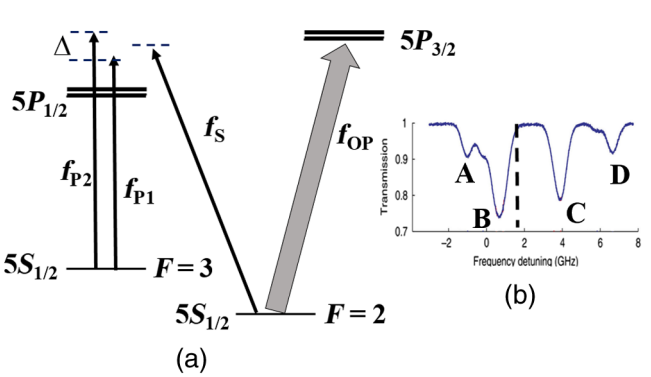

Fig. 12 ^{85}Rb transitions: (a) the experiment scheme and (b) the linear absorption spectrum of ^{85}Rb and ^{87}Rb. The dashed line indicates the frequency of f_{p1}.

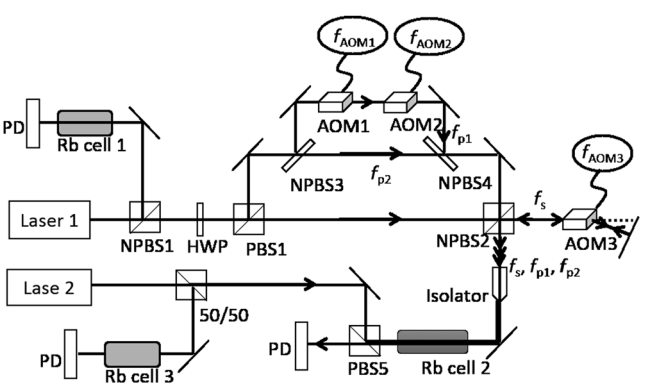

Fig. 13 The experimental setup of double-Raman gain. Laser 1 is a Ti-Sapphire laser operating at 795 nm. Laser 2 is a diode laser with tapered amplifier operating at 780 nm. See text for details.

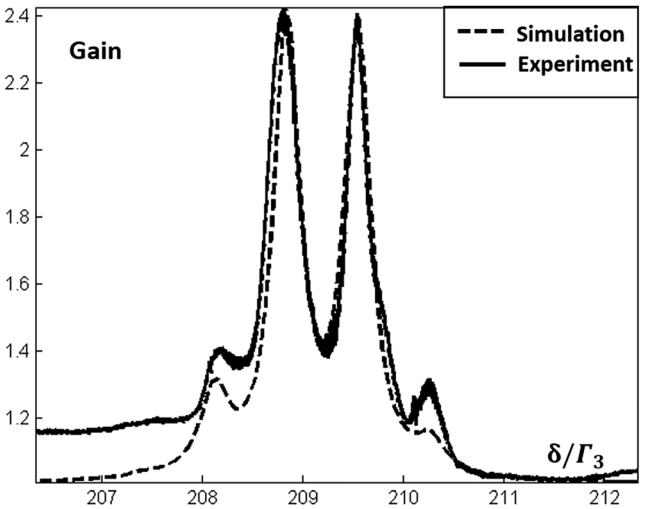

Fig. 14 Experimental data versus simulation results. See text for details.

that this laser remained resonant with the $5S_{1/2}$, $F = 2 \rightarrow 5P_{3/2}$ transition in ^{85}Rb. The light passing through NPBS5 was then reflected by PBS2 into the primary cell.

The solid line in Fig. 14 shows a typical experimental result obtained with this setup. The vertical axis shows the gain experienced by the probe. The horizontal axis is the frequency of the probe, expressed in term of δ/Γ_3, where Δ_p is the mean detuning of the two Raman pumps [see Fig. 12(a)], δ is the detuning of the Raman probe, and Γ_3 is the radiative linewidth of the intermediate state, which is $\sim 2\pi * 6 * 10^6$ s^{-1}. For this data, we have $\Delta_p/\Gamma_3 \sim 200$ and $\Delta/\Gamma_3 = 1.365$. The cell was heated to ~90°C, corresponding to a density of $\sim 2 * 10$ m^{-3}.[24] The power in the first Raman (lower frequency) pump was 48.4 mW, and that in the second Raman pump was 12.9 mW. The power in the probe beam was 150 μW. The diameter of the probe was about the same as that of the first Raman pump ($d_{\text{pump1}}/d_{\text{probe}} \cong 1$), while the diameter of the second Raman pump was somewhat bigger ($d_{\text{pump1}}/d_{\text{pump2}} \cong 0.75$).

The dashed line in Fig. 14 shows the result of the simulation corresponding to this data. Here, we increased the value of M until a stable result was obtained for $M \geq 7$. The plot shown corresponds to $M = 7$. For the simulation, we have used the pump and probe powers listed above, and used the same ratios for the beam diameter as shown above. However, the actual size of the diameter for the first Raman pump was used as a fitting parameter. This was necessary because the absolute calibration of the beam profile used to measure the beam diameters was somewhat inaccurate. A value of $d_{\text{pumps}} \cong 1.4$ mm produced the plot shown here. We also assumed that the transition strength for each leg of the Raman transition is the same, with a saturation intensity that is 1.5 times larger than that for the strongest (cycling) transition in the D2-manifold of ^{85}Rb (i.e., the $F = 3$, $m_F \rightarrow F' = 4$, $m_F = 4$ transition). This is an approximation based on considering all different Zeeman sublevels that actually contribute to the Raman transition for the cross linear polarization used. A more accurate calculation would have been to keep track of all the Zeeman sublevels explicitly and will be carried out in the near future. Similarly, we have used an approximated value of $\Gamma_{12} \cong 0.35\Gamma_3$, while the maximum possible value of this rate is $\sim 0.5\Gamma_3$. The peak value of the gain for the simulation was found to be ~2.4. However, the peak value of the gain observed experimentally was somewhat uncertain due to some imprecision in the measurement of the amplified and unamplified probe power.

5 Conclusion

In this paper, we have presented a detailed model for computing the gain profile generated by a pair of Raman pumps applied to a Λ-type system, for the condition where the pumps are allowed to be very strong with an arbitrarily small difference frequency. Specifically, we have developed a code that enables one to keep track of an arbitrarily large number of high order harmonics that result from the interference between the two pumps. We have verified the validity of these codes by considering many limiting conditions. We then used this code to understand the behavior of the gain profile for a wide range of conditions. We have also identified the condition under which the Raman gain saturates. Specifically, we have shown that the gain saturation occurs when the effective two-photon transition process, mediated by the mean value of the two Raman pump fields and the probe field, reaches a transition rate that equals the rate of optical pumping used to produce the Raman population inversion. A nontrivial conclusion of this finding is that the Raman probe beam can become much stronger than each of the pump beams under properly chosen parameters. We also describe an experimental setup for producing a double-Raman gain using a Rb vapor cell, under the conditions where higher harmonics become significant in the gain profile. We find the prediction of one model agrees well with the experimental result. The model presented here is likely to be very useful in developing a numerical code for a superluminal laser under a wide range of conditions.

Acknowledgments

This work was supported in part by the AFOSR Grant No. FA9550-10-1-0228 and NASA Grant No. NNM13AA60C.

References

1. H. N. Yum et al., "Superluminal ring laser for hypersensitive sensing," *Opt. Express* **18**(17), 17658–17665 (2010).
2. M. S. Shahriar et al., "Ultrahigh enhancement in absolute and relative rotation sensing using fast and slow light," *Phy. Rev. A* **75**, 053807 (2007).
3. G. S. Pati et al., "Demonstration of displacement-measurement-sensitivity proportional to inverse group index of intra-cavity medium in a ring resonator," *Opt. Commun.* **281**, 4931–4935 (2008).
4. G. S. Pati et al., "Demonstration of a tunable-bandwidth white light interferometer using anomalous dispersion in atomic vapor," *Phys. Rev. Lett.* **99**, 133601 (2007).
5. M. S. Shahriar and M. Salit, "Application of fast-light in gravitational wave detection with interferometers and resonators," *J. Mod. Opt.* **55**, 3133 (2008).
6. D. D. Smith et al., "Dispersion-enhanced laser gyroscope," *Phys. Rev. A* **78**, 053824 (2008).
7. D. D. Smith et al., "Enhanced sensitivity of a passive optical cavity by an intracavity dispersive medium," *Phys. Rev. A* **80**, 011809(R) (2009).
8. D. D. Smith et al., "Fast-light enhancement of an optical cavity by polarization mode coupling," *Phys. Rev. A* **89**, 053804 (2014).
9. O. Kotlicki, J. Scheuer, and M. S. Shahriar, "Theoretical study on Brillouin fiber laser sensor based on white light cavity," *Opt. Express* **20**(27), 28234 (2012).
10. L. J. Wang, A. Kuzmich, and A. Dogariu, "Gain-assisted superluminal light propagation," *Nature* **406**, 277–279 (2000).
11. J. S. Toll, "Causality and the dispersion relation: logical foundation," *Phys. Rev.* **104**, 1760–1770 (1956).
12. A. Wicht et al., "White-light cavities, atomic phase coherence, and gravitational wave detectors," *Opt. Commun.* **134**, 431–439 (1997).

13. R. H. Rinkleff and A. Wicht, "The concept of white light cavities using atomic phase coherence," *Phys. Scr. T* **118**, 85–88 (2005).
14. R. Fleischhauer and J. Evers, "Four wave mixing enhanced white-light cavity," *Phys. Rev. A* **78**, 051802(R) (2008).
15. H. Wu and M. Xiao, "White-light cavity with competing linear and nonlinear dispersions," *Phys. Rev. A* **77**, 031801(R) (2008).
16. A. Rocco et al., "Anomalous dispersion of transparent atomic two- and three-level ensembles," *Phys. Rev. A* **66**, 053804 (2002).
17. T. Laupretre et al., "Anomalous ring-down effects and breakdown of the decay rate concept in optical cavities with negative group delay," *New J. Phys.* **14**, 043012 (2012).
18. T. Laupretre et al., "Photon lifetime in a cavity containing a slow-light medium," *Opt. Lett.* **36**(9), 1551–1553 (2011).
19. J. Schaar, H. Yum, and M. S. Shahriar, "Theoretical description and design of a fast-light enhanced helium-neon ring-laser gyroscope," *Proc. SPIE* **7949**, 794914 (2011).
20. H. N. Yum et al., "Demonstration of white light cavity effect using stimulated Brillouin scattering in a fiber loop," *J. Lightwave Technol.* **31**(23), 3865–3872 (2013).
21. M. O. Scully and W. E. Lamb, *Laser Physics*, Westview Press, Boulder, Colorado (1974).
22. M. O. Scully and M. S. Zubairy, *Quantum Optics*, Cambridge University Press, New York (1997).
23. M. S. Shahriar et al., "Evolution of an N-level system via automated vectorization of the Liouville equations and application to optically controlled polarization rotation," *J Mod. Optic.* **61**(4), 351–367 (2014).
24. D. A. Steck, "Rubidium 85 D line data," http://steck.us/alkalidata/rubidium85numbers.pdf (17 May 2015).

Ye Wang received his BS degree in optical engineering from Zhejiang University in 2008. Currently, he is a PhD student in the Department of Electrical Engineering and Computer Science (EECS) at Northwestern University, working in the Laboratory for Atomic and Photonic Technology under Professor Selim Shahriar. His research is focused on investigation of ultra-low light level nonlinear optics using tapered nanofiber and the application of anomalous dispersion for precision metrology.

Zifan Zhou received his BS degree in electrical engineering from Huazhong University of Science and Technology in 2012. Currently, he is a PhD student in electrical engineering at Northwestern University, working in the Laboratory for Atomic and Photonic Technology under Professor Selim Shahriar. His research is focused on applications of slow and fast light as well as gravitational wave detection.

Joshua Yablon received his BS degree in engineering physics at Cornell University in 2007. Currently, he is a PhD student in electrical engineering at Northwestern University, working in the Laboratory for Atomic and Photonic Technology under professor Selim Shahriar. His research is focused on application of fast light for precision metrology, as well as gravitational wave detection.

Selim Shahriar is a professor in the Departments of EECS and Physics and Astronomy at Northwestern University. His received his PhD from MIT in 1992. His research interests include applications of slow and fast light, quantum computing, gravitational wave detection, tests of general relativity, holographic and polarimetric image processing, atomic clocks, and atom interferometry. He has published 403 journal and conference papers. He is a fellow of SPIE and OSA.